Thermal lag analysis on a simulated TGA-DSC device

Roberto Comesaña *, Miguel A. Gómez, Miguel A. Álvarez, Pablo Eguía

Escuela Ingeniería Industrial, University of Vigo, Campus Lagoas-Marcosende, 36310 Vigo, Spain

A B S T R A C T

A ThermoGravimetric Analyser with Differential Scanning Calorimeter (TGA-DSC) has been simulated to evaluate the influence of different parameters on thermal lag. Two virtual materials with selected properties were created and combined with two heating rates. A three-dimensional mesh was created based on measurements in the actual TGA-DSC. Specific models have been applied and boundary conditions have been configured, including a programmed Proportional Integral Derivative (PID) controller to regulate temperature. The results showed that a sample with a lower thermal diffusivity had greater temperature differences when compared to the furnace temperature than a sample with a higher thermal diffusivity. Biot number has also been computed to analyse temperature differences within the sample. Thermal diffusivity and Biot number effects were miniscule compared to the heating rate, which increased sample temperature instability and temperature differences within the sample.

© 2012 Elsevier B.V. All rights reserved.

1. Introduction

Biomass combustion is the primary focus of our research group. The fuel has different origins and compositions depending on its type, supplier, batch and storage conditions, making it necessary to know the detailed composition in order to characterise it. An external laboratory performed a statistical analysis on a regular basis but, to increase the frequency of analysis and open new research possibilities regarding detailed experimental conversion data, a TGA-DSC (ThermoGravimetric Analyser with Differential Scanning Calorimeter) and a FTIR (Fourier Transformed InfraRed Spectrometer) analyser were acquired.

The TGA consists of two crucibles held in a furnace within a controlled environment, as shown in Fig. 1. The fuel sample is located in one of the upper crucibles and the other one is used as reference. Both of them sit on a bracket that rests on a precision balance external to the furnace to protect the balance from high temperatures. A gas inlet conductor is placed on the base of the system to guide sweeping gas. Several layers are arranged on the exterior of the furnace including a ceramic wall, an electric resistance, an isolating layer, a protective argon chamber and a water chamber for refrigeration. The sample undergoes a user-defined thermal cycle, and the loss of mass and the heat flux exchanged through the system are measured.

The FTIR allows the gases exiting the TGA-DSC to be measured qualitatively and quantitatively. Several tests and a modification in the TGA-DSC [1] were required to couple it with the FTIR, but this

adjustment allowed for improvement of the measurements taken [2] and allowed for their use in biomass characterisation.

However, the need to control experimental conditions within desirable parameters led to the present focus on the SETARAM LABSYS TGA-DSC working principles [3].

In the TGA-DSC, three thermocouples are located in the furnace: one centred on the bracket and two of them under the crucibles on the same bracket, integrated in the DSC measuring device, as shown in Fig. 2. The central thermocouple measures the temperature in the centre of the upper volume of the furnace, which is assumed to be the average furnace temperature. The system of thermocouples located under the crucibles is employed to obtain DSC heat flux data. The desired thermal cycle is input into the control system of the device, which uses the central thermocouple temperature to adjust the power supplied to the electrical resistance. Thus, the temperature evolution in the furnace matches the set point value. Small differences and mass data due to furnace characteristics are corrected before each test by performing a blank test with no sample in the crucible. The blank test allows subtracting the unexpected measurements of mass variation and DSC that may take place during the thermal cycle with no sample due to uncontrolled events related with temperature evolution, such as buoyancy effects or small DSC signals due to heat flux imbalances between crucibles.

The sample is placed in a 100 mm³ platinum crucible. A small amount of the representative compound is generally used in order to avoid complications that may arise when the amount of mass is increased, such as the intensification of thermal lag effects, even at low heating rates. However, even when a small mass is used as a sample, its local temperature can differ from the furnace temperature. This usually appears as a delay known as thermal lag [4]. The thermal lag effect has been taken into account in several

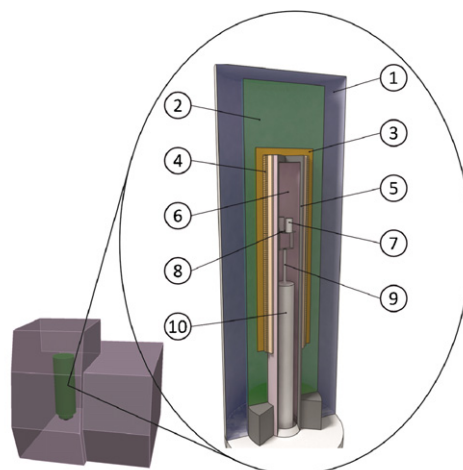* Corresponding author. Tel.: +34 986818624.
  E-mail address: robcomesana@uvigo.es (R. Comesaña).

Nomenclature

a_g	absorption coefficient
B_i	Biot number
C_p	specific heat capacity
e	PID error
$E_{f,s}$	energy flux to the sample
$E_{\Delta T}$	energy stored as sensible heat
$\vec{F}$	external body forces
$\vec{g}$	gravity vector
h	enthalpy
h_t	convective heat transfer coefficient
Δh_{mel}	latent heat of fusion
I_t	unit tensor
I	radiation intensity
$\vec{J}_J$	diffusion flux of species j
k	thermal conductivity
Kd	PID derivative constant
Ki	PID integral constant
Kp	PID proportional constant
L_c	characteristic length
M	molar mass
n	refractive index
P	pressure
P_{vp}	operating pressure
$\vec{r}$	radiation position vector
R	ideal gas constant
$\vec{s}$	radiation direction vector
S_m	mass source
Sh	volumetric heat sources
t	time
t_k	time at actual time step
t_{k-1}	time at previous time step
t_{k-2}	time 2 time steps before
Δt	time step size
T	temperature
T_{mel}	melting temperature
T_s	cell temperature
u	PID controller output
$\vec{v}$	velocity vector
v_i	velocity component in direction i
V	volume
x_i	i coordinate
x_k	k coordinate
Y_{liq}	liquid mass fraction
α	thermal diffusivity
μ	molecular viscosity
ρ	density
σ	Stefan–Boltzmann constant
σ_s	scattering coefficient
τ_{ij}	stress tensor
ϕ	scattering function
Ω	solid angle

1- Water chamber, 2- Argon chamber, 3- Isolating layer,
4- Electrical heating resistor, 5- Furnace ceramic wall,
6- Furnace interior, 7- Crucible, 8- Base with thermocouples,
9- Bracket, 10- Gas inlet conduction

Fig. 1. TGA-DSC layout.

heating rate influence the amount of thermal lag and, moreover, can affect other measurements such as the kinetic evaluations of mass loss curves [12] versus temperature.

The biomass samples undergo several processes: drying, pyrolysis and char combustion, when oxygen is present in the furnace atmosphere. Some of these processes are endothermic, others are exothermic and have different kinetics and complex mechanisms. As sample temperature needs to be known at all times during the study of these processes, the unknown thermal lag needs to be analysed to assess its influence on the data obtained. However, the
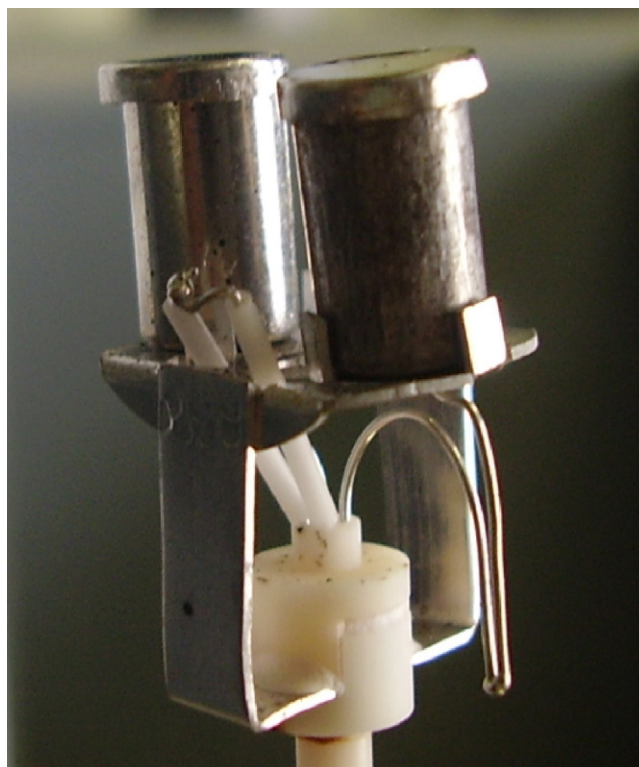

Fig. 2. Bracket and thermocouples.

studies regarding biomass pyrolysis [5–7]. When the thermal lag is not detected, the sample is assumed to be at the furnace temperature. Undetected thermal lag has been considered to be the origin of the compensation effect [8] in biomass pyrolysis, which is based on a linear relationship between enthalpies and entropies of different reactions [9]. However, some authors do not share this conclusion [10,11] and defend that the compensation effect is independent of thermal lag.

The amount of thermal lag that develops is dependent on several variables. It is known that parameters such as sample size and

Table 1
Thermal lag simulation test data.

Property [units]\test	A05	A50	B05	B50
Conductivity [W/m K]	0.05	0.05	400	400
Density [kg/m^3]	10^4	10^4	10^4	10^4
Heat capacity [J/kg K]	800	800	800	800
Thermal diffusivity [m^2/s]	6.3×10^{-9}	6.3×10^{-9}	5×10^{-5}	5×10^{-5}
Melting point [K]	400	400	400	400
Latent heat of fusion [J/kg]	2×10^4	2×10^4	2×10^4	2×10^4
Sample mass [mg]	79.36	79.36	79.36	79.36
Sample volume [mm^3]	7.94	7.94	7.94	7.94
Heating rate [K/min]	5	50	5	50
Time step size [s]	5	5	5	5
Initial temperature [K]	300	300	300	300
Final temperature [K]	500	500	500	500
Simulated time [s]	2650	275	2650	275

Fig. 3. Two-dimensional mesh overview and crucibles detail.

accurate measurement of the sample temperature is not possible without a certain error, so this thermal lag is often present.

Therefore, in order to evaluate the influence of different parameters on thermal lag, a simulation of a TGA-DSC was carried out. Because simulation conditions were controlled and properties were clearly defined, the influence of different sample characteristics could be analysed. The main advantage of this approach was the possibility to calculate the temperature within the sample, which allowed the internal conditions of the sample to be known during the entire thermal cycle.

Because it is common to use a small sample inside these devices, variations due to different masses and volumes were neglected. The material was a solid that melted at an intermediate temperature. Two heating rates were employed so that the temperature lag could be observed. The lower heating rate was 5 K/min, an order of magnitude employed for phase change tests. The higher heating value was 50 K/min, a value near the maximum allowed by the real equipment.

Two sample materials were defined to obtain two thermal diffusivity values and were labelled as A and B. Thermal diffusivity is a reference datum for the thermal inertia of the sample and it is defined by material properties, as shown in Eq. (1), where k is the thermal conductivity, ρ is the density and C_p is the specific heat capacity. Material properties were selected so that the two thermal diffusivities obtained were quite different. The lower value (material A) is 6.3×10^{-9} m^2/s, an order of magnitude below wood, oil or Nylon. This implies that thermal conductivity is significantly lower than the energy storing capacity, so higher temperature differences between the sample and the environment will be likely to appear. The higher value for thermal diffusivity (material B) is 5×10^{-5} m^2/s, which falls within a common range for many metals and gases such as air, argon, nitrogen, aluminium, steel or iron [13].

$$\alpha = \frac{k}{\rho \cdot C_p} \tag{1}$$

The selected higher and lower thermal diffusivity values combined with the selected heating rates led to four different simulations. Only heating rate and thermal diffusivity are varied, while the rest of the parameters are kept constant to isolate the effect of the desired parameters on thermal lag. To match the aforementioned requirements, two virtual materials were created that were combined with two heating rates. Table 1 summarises the most important characteristics that result from different combinations of heating rates and thermal diffusivities.

By varying these parameters, the sample thermal condition is significantly different, and its effect on the thermal lag can be analysed.
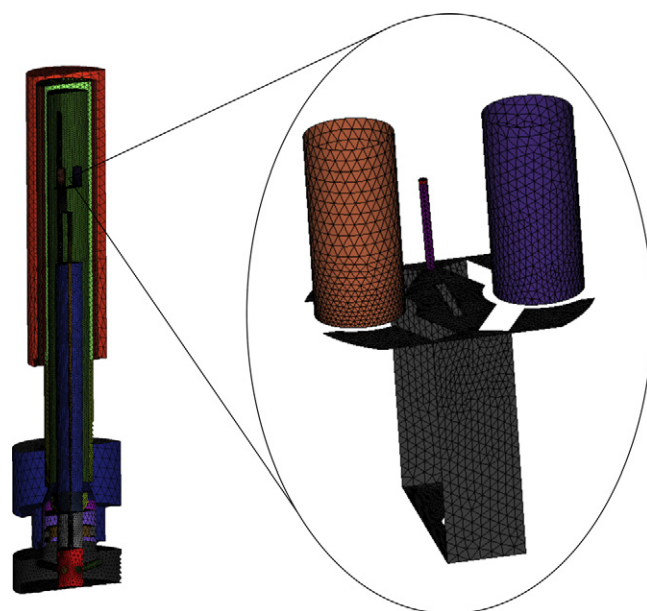
2. Modelling

The first step for the simulation setup was to create the geometric model. Necessary dimensions were measured on the actual equipment and a realistic but slightly simplified CAD model was created.

Based on the virtual model, the relevant surfaces were converted into two-dimensional meshes, as shown in Fig. 3. A three-dimensional mesh was created based on the aforementioned two-dimensional mesh. Both the walls and the volumes generated were labelled, and specific boundary conditions were applied as described in Section 2.1.

The simulation configuration includes models that compute gas movement over the domain (laminar flow), conduction through the walls, convection with the surrounding surfaces and radiation. The equations included in these models are presented in Section 2.2. The main parameters are summarised in Tables 1 and 2 for the domain materials and in Table 3 for the boundary conditions.

The simulation of buoyancy in the water and argon chambers limited the time step size dramatically, which can result in an increased delay in the simulation time. Therefore, the argon

Table 2
Material properties employed in the simulation (data obtained from ANSYS FLUENT 13 and online databases).

Material	Density [kg/m^3]	Specific heat capacity [J/kg K]	Thermal conductivity [W/m K]
Aluminium	2719	871	202.4
Felt insulation	100	1380	0.0399
Nichrome (electrical resistance)	8400	450	11.3
Aluminium oxide	386	850	30
Platinum (crucibles)	21,450	130	71.599
Steel	8030	502.5	16.27
Nitrogen	Incompressible ideal gas	Polynomial: $938.89917 + 0.301791 \cdot T - 8.1092279e-05 \cdot T^2 + 8.2638918e-09 \cdot T^3 - 1.537235e-13 \cdot T^4$	0.0242

Table 3
Summary of boundary conditions.

Boundary	Configuration	Value
Inlet	Mass flow inlet	N_2 $T = 300$ K, flow $= 9.48 \times 10^{-7}$ kg/s
Outlet	Outflow	–
External walls	Convection	$T = 300$ K, $h = 15$ W/m^2 K
Walls in contact with argon chamber	Convection	$T = 292$ K, $h = 5.7$ W/m^2 K
Internal walls	Coupled	–

and water chambers were suppressed and replaced by a global heat transfer coefficient. This simplifies the model and significantly reduces the simulation time without varying the original condition of the furnace. Several simulations were performed to compute the global coefficient. Virtual tests with and without this simplification led to similar results, indicating that the modification did not change the real conditions.

2.1. Boundary conditions

A complete set of boundary conditions was applied to simulate the real working characteristics of the TGA-DSC.

The sweeping gas was nitrogen (N_2), which entered the furnace at 300 K at a rate of 9.48×10^{-7} kg/s (equivalent to 50 mL/min) through a mass flow inlet. Additionally, an outlet was configured as the outflow condition.

The walls were divided in various groups. The walls that were in contact with ambient air received a convection coefficient of 15 W/m^2 K and an external temperature of 300 K. Additionally, the walls inside the argon chamber were configured with the aforementioned global heat transfer coefficient that includes the combined effect of argon and refrigerated water. This was introduced to the simulation by a convection condition with an external temperature of 292 K and a convection coefficient of 5.7 W/m^2 K. The remaining walls were defined as coupled, which allowed the convection on both sides of the wall and the conduction through the wall to be computed by the software based on the material properties and the interaction between the wall and the fluid. A summary of aforementioned conditions is shown in Table 3.

The simulated and real TGA-DSCs should operate identically. Therefore, the heating process has also been programmed in the simulation similarly to the temperature control in the experimental equipment. The heating electrical resistance power W/m^3 was continuously governed by a Proportional Integral Derivative (PID) controller based on the temperature data of the central thermocouple and the desired set point [14], as shown in Eq. (2):

$$u(t) = Kp \cdot e(t) + Ki \cdot \int e(t)dt + Kd \cdot \frac{d(e(t))}{dt} \tag{2}$$

To be programmed, the control loop was discretised by employing the backward Euler method [15], as shown in Eq. (3):

$$u(t_k) = u(t_{k-1}) + Kp \cdot [e(t_k) - e(t_{k-1})] + Ki \cdot \Delta t \cdot e(t_k)$$
$$+ \frac{Kd}{\Delta t} \cdot [e(t_k) - 2 \cdot e(t_{k-1}) + e(t_{k-2})] \tag{3}$$

The PID output should positively coincide with the set point, and so the three constants that control the output needed to be properly adjusted. A simulation was configured in which the thermal resistance was fixed at its maximum power and the temperature evolution in the central thermocouple was monitored. This data allowed the transfer function to be obtained, which was employed in a Matlab Simulink [16] program that found the optimum constants, shown in Table 4.

Table 4
Optimised PID constants.

Kp	Ki	Kd
4.3217	0.042	174.6861

This model was implemented and the power on the electrical resistance was regulated based on a two-row matrix with time values in the first row and normalised desired temperatures in the second.

2.2. Models

Several models were employed in the simulation, both embedded on the commercial CFD code ANSYS FLUENT 13 (shown in Table 5) and developed by the authors [17]. Those models account for the laws that must be satisfied in every cell that belongs to the furnace domain. Laminar conditions were applied to the gas movement inside the furnace due to the low velocity present over the entire domain under the experimental conditions selected.

A melting model was developed that allows the solid to melt when heated and, if required, allows the liquid to return to solid phase as the temperature decreases. The sample temperature in each cell was allowed to exceed the melting temperature when heating and to decrease below it when cooling. At the end of each time step, the energy stored by the cell as sensible heat was computed using Eq. (4), where T_s and T_{mel} are the sample and melting temperatures, respectively. The heat capacity employed is constant and its value is shown in Table 1.

$$E_{\Delta T} = C_p \cdot (T_s - T_{mel}) \cdot \rho \cdot V \tag{4}$$

This energy was employed in melting or solidifying the sample in the cell. The liquid mass fraction was increased or decreased according to Eq. (5), based on the energy computed in Eq. (4), and the temperature of the cell was fixed at the melting temperature. In this process, sensible heat is converted into latent heat or vice versa [18].

$$Y_{liq}(t + \Delta T) = Y_{liq}(t) + \frac{E_{\Delta T}}{\Delta h_{mel} \cdot \rho \cdot V} \tag{5}$$

When the whole cell phase conversion was completed, the cell temperature evolved according to the amount of energy exchanged and its heat capacity. These equations model the phase transition in the four tests which were simulated.

3. Results and discussion

Firstly, a check on temperature evolution inside the TGA-DSC was performed. In Fig. 4, the temperature measured by the

Table 5
Embedded ANSYS FLUENT 13 models employed in the simulation.

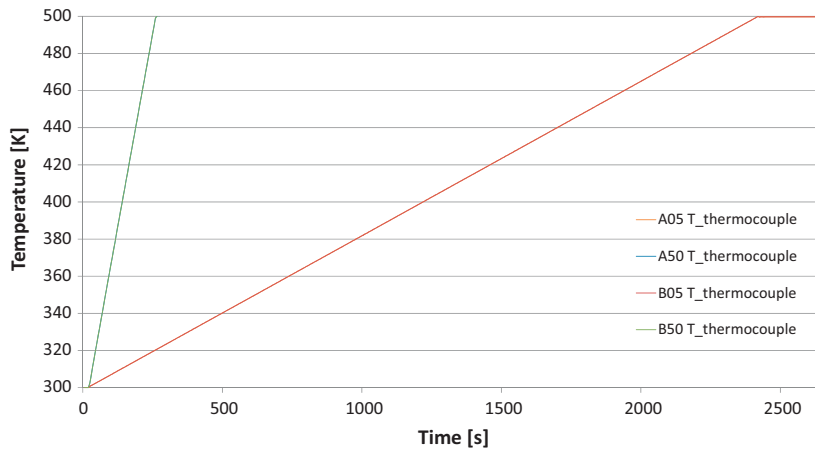| Model	Equation
Mass conservation	$\frac{\partial \rho}{\partial t} + \nabla(\rho\vec{v}) = S_m$
Incompressible ideal gas density	$\rho = \frac{P_{vp} \cdot M_w}{T \cdot R}$
Laminar flow (Navier–Stokes)	$\frac{\partial}{\partial t}(\rho\vec{v}) + \nabla(\rho\vec{v}\vec{v}) = -\nabla(p) + \nabla \cdot \left\{ \mu \left[(\nabla\vec{v} + \nabla\vec{v}^T) - \frac{2}{3}\nabla \cdot \vec{v}I \right] \right\} + \rho\vec{g} + \vec{F}$
Energy	$\frac{\partial}{\partial t}(\rho h) + \frac{\partial}{\partial x_i}(\rho u_i h) = \frac{\partial}{\partial x_i}(k)\frac{\partial T}{\partial x_i} - \frac{\partial}{\partial x_i}\sum_j h_j\vec{J}_j + \frac{\partial p}{\partial t} + (\tau_{ij})\frac{\partial u_i}{\partial x_k} + S_h$
Radiation discrete ordinates	$\nabla(I(\vec{r}, \vec{s})\vec{s}) = -(a_g + \sigma_s)I(\vec{r}, \vec{s}) + \frac{a_g \cdot n^2}{\pi}\sigma T^4 + \frac{\sigma_s}{4\pi}\int_0^{4\pi} I(\vec{r}, \vec{s}')\phi(\vec{s} \cdot \vec{s}')d\Omega$

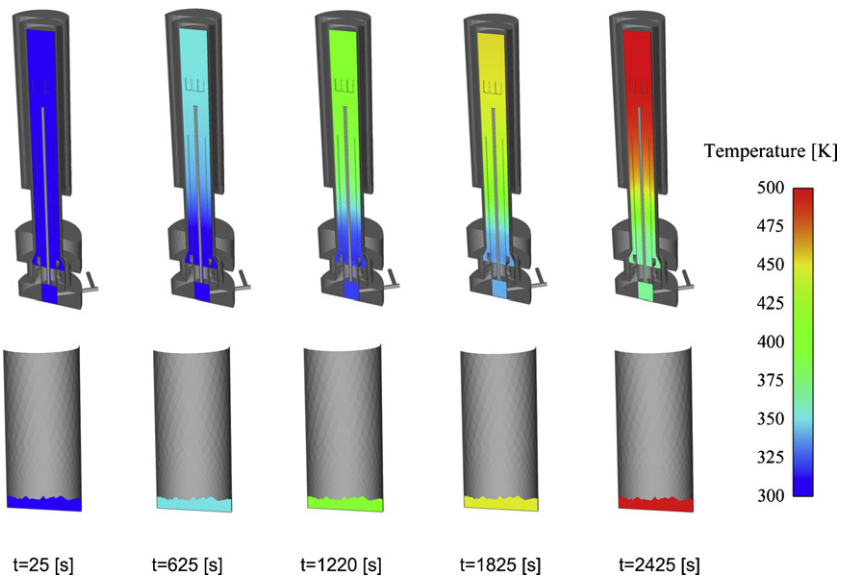**Fig. 4.** Central thermocouple temperature versus time.

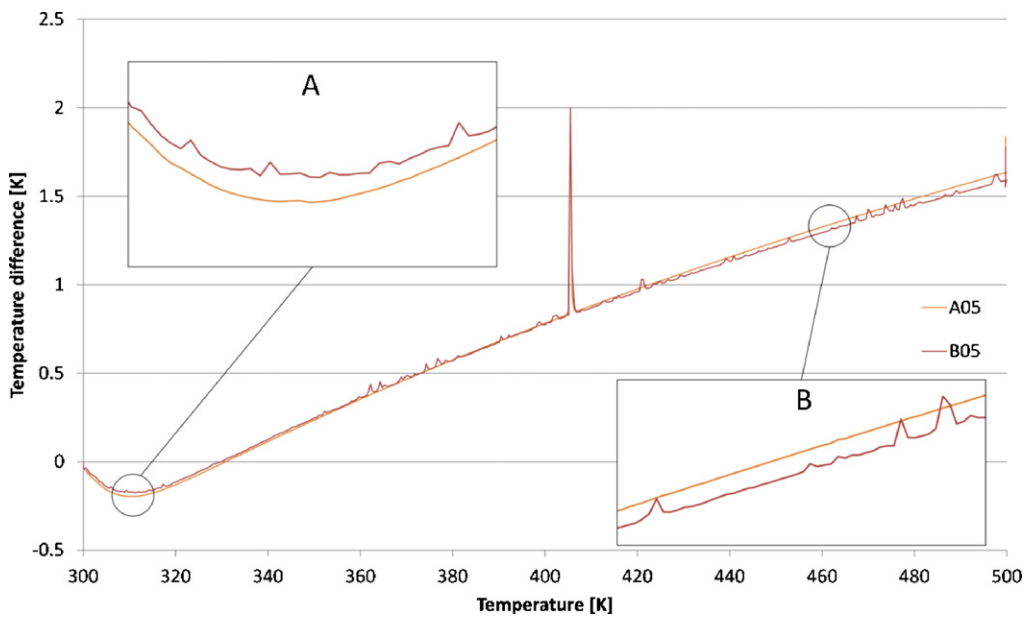**Fig. 5.** Furnace and sample temperature contours in test A05.

Fig. 6. Difference between furnace and sample temperature versus furnace temperature on 5 K/min tests.
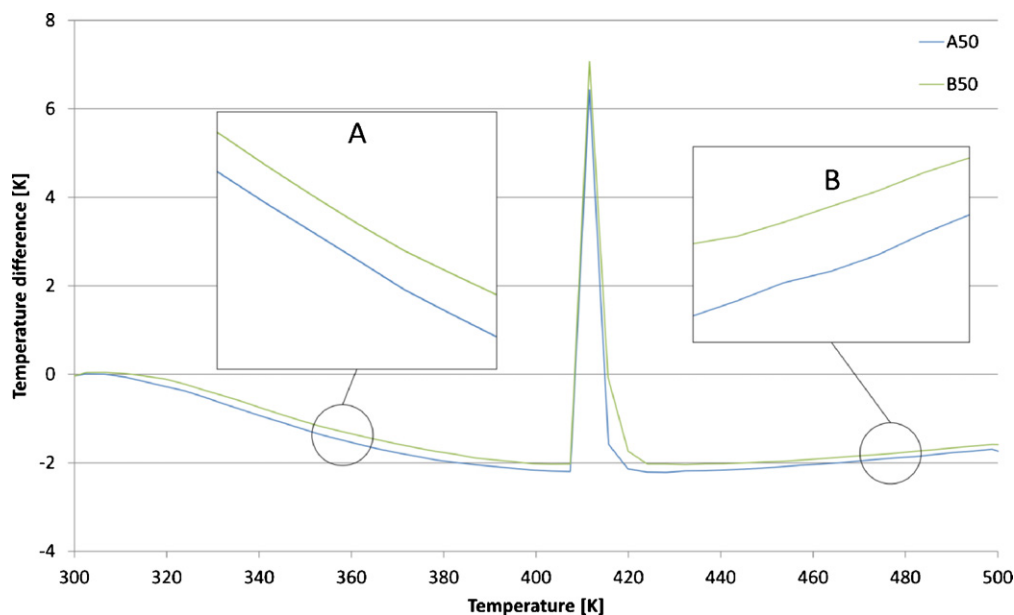
Fig. 7. Difference between furnace and sample temperature versus furnace temperature on 50 K/min tests.

central thermocouple in the furnace was plotted as a function of time. Two groups were shown: tests at 5 K/min (A05 and B05) and 50 K/min rates (A50 and B50). Both tests are based on a set point that includes three phases: a short period of time at the beginning to stabilise temperature, a constant rate temperature increase up to 500 K and a constant temperature at 500 K. The TG-DSC can work up to 1300 K, but the range of interest was centred on the latent heat exchange temperatures, where the greatest differences arouse. The maximum temperature was limited to 500 K to avoid increasing the tests duration and the computational cost. The temperature set point was matched in both scenarios, and remarkable repeatability was achieved for both tests with the same rate.

The temperature on the TGA-DSC was also presented using contours in Fig. 5, next to the sample temperature. The evolution was similar in both the sample and the furnace, but a more detailed approach was required.

For the 5 K/min tests, the difference between furnace temperature and average sample temperature versus furnace temperature is shown in Fig. 6, and details on particular ranges are presented in details A and B. The data plotted as furnace temperature are always values of the central thermocouple. For both tests, the sample heated faster than the thermocouple in the beginning, but after reaching a temperature of 330 K, the sample temperature was lower. This difference reaches a maximum at 400 K during the latent heat absorption, where the peak is formed. After the peak, the temperature difference was higher than before and increased as the test advances.

Thermal diffusivity values indicated that sample B would be closer to furnace temperature, as shown in the details A and B in Fig. 6. In addition, sample B was more sensitive to heat release from the electrical resistance, and its temperature fluctuated.

The same analysis was performed for the 50 K/min tests, as shown in Fig. 7. With this heating rate, the sample temperature
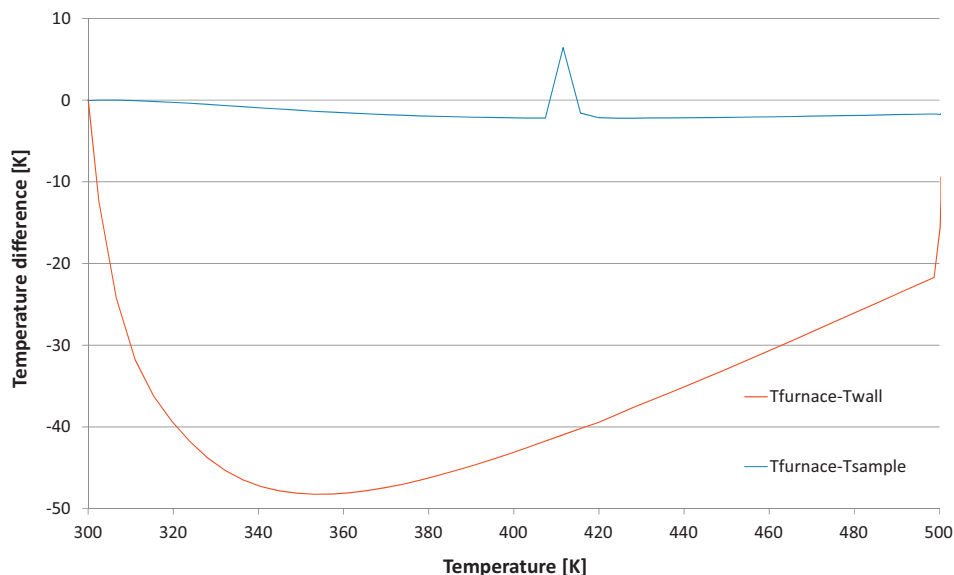

Fig. 8. Difference between furnace temperature and sample and wall temperatures for A50 test.
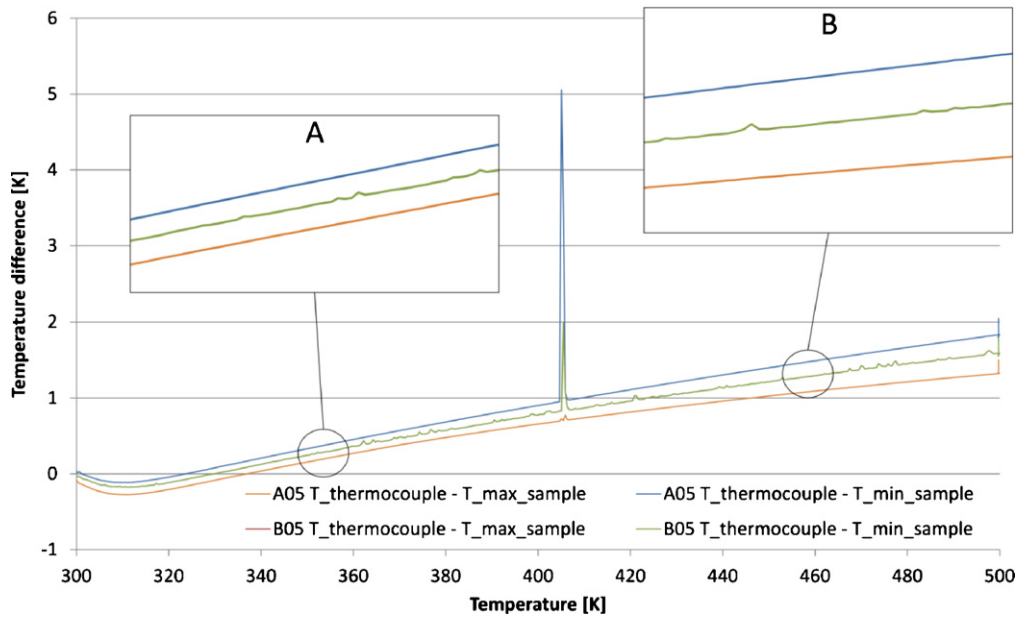
Fig. 9. Differences between furnace and sample maximum and minimum temperatures versus furnace temperature on 5 K/min tests.

was usually higher than the furnace temperature. During the phase change, there was also peak showing the delay between the sample and furnace temperatures due to the latent heat absorption. Two representative ranges are shown in details A and B in Fig. 7.

A possible explanation for a higher sample temperature is the incidence of radiation due to a higher temperature in the furnace wall as a result of the higher power required in the electrical resistance to achieve the desired rate. Despite the low temperature differences, the radiation can influence the sample temperature because of the small sample mass and the proximity between the crucibles and the walls due to the compactness of the furnace. Also, the crucible surface is considerably larger than the thermocouple surface, so the radiation effects are expected to be stronger in the crucible. The differences between the furnace temperature and the wall and sample temperatures for A50 test are shown in Fig. 8.

However, mean sample temperature did not reveal all the information about the process. The Biot number was computed for both samples according to Eq. (6), based on an average heat transfer coefficient computed by simulation, the geometric data and its properties. The Biot number is a dimensionless index that compares the importance of the heat transfer by convection on the surface of the body and the conduction through its interior. It determines the magnitude of the temperature gradient that is created in the interior of the body when a heat flux is applied.

$$B_i = \frac{h_t \cdot L_c}{k} \tag{6}$$

The values obtained were 1.06×10^{-3} for sample A and 1.32×10^{-7} for sample B. Both indicated that an assumption of an isothermal sample was allowed, but slight differences were clear when details were analysed. Firstly, 5 K/min rates were studied, as shown in Fig. 9, where sample maximum and minimum temperatures were plotted versus furnace temperature. Sample B, with a lower Biot number, had a homogeneous temperature over the whole range, while sample A showed differences between maximum and minimum temperatures, as shown in details A and B in Fig. 9.

This effect was compared for the same furnace temperature in the contours of Fig. 10. For sample A, with a higher Biot number, the temperature gradient was greater.

The same analysis was performed for the 50 K/min tests. Similarly, sample A showed greater temperature differences, as presented in Fig. 11 and is enhanced in the details A and B.

The differences in the temperature gradients are presented using contours in Fig. 12, where sample A again shows greater differences. This indicates that a lower thermal diffusivity created a greater delay between the furnace temperature and sample A. Due to the influence of heat convection in the furnace and geometric sample characteristics, a higher Biot number was also present for this sample and greater temperature gradients were obtained.

Comparing the two rates, a higher rate was observed to create more instability between the sample and furnace temperatures and increases the temperature differences within the sample, as shown in Figs. 11 and 9.

According to Eqs. (4) and (5), the liquid mass fraction is computed for each cell. The volume average liquid mass fraction is computed for each time step and is shown in Figs. 13 and 14. The effect of the thermal lag was present in the phase change
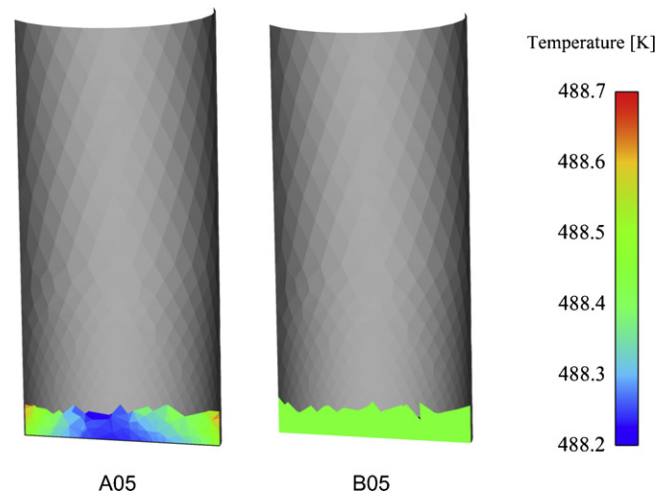

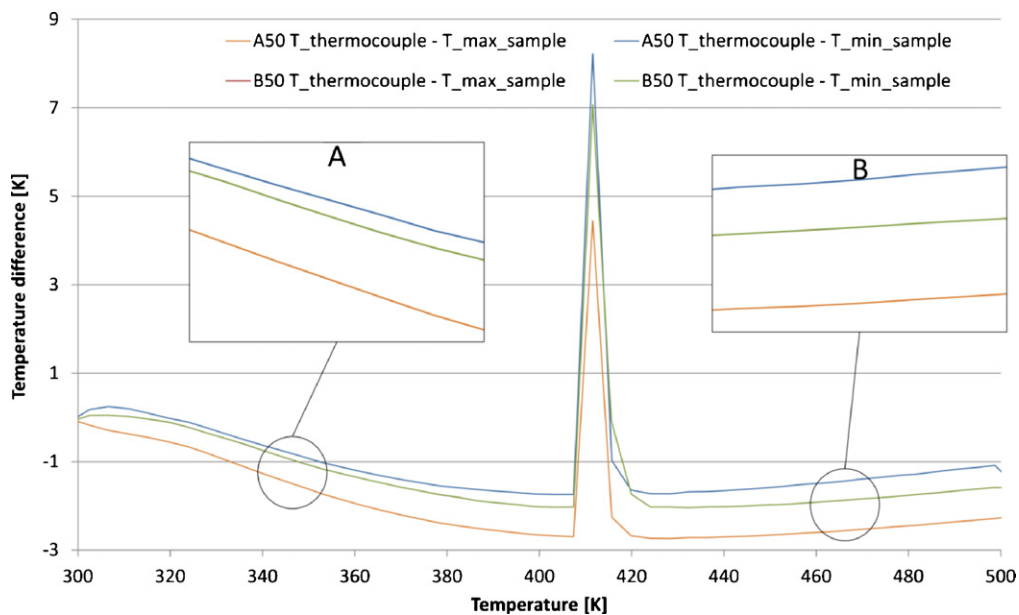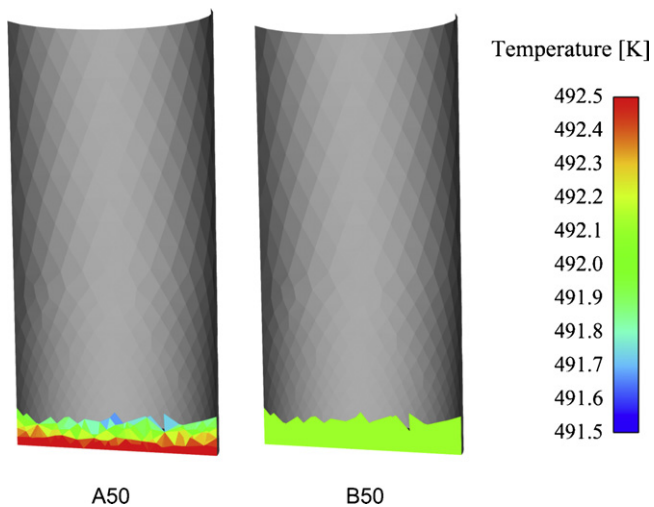Fig. 10. Sample temperature gradient in 5 K/min tests.

Fig. 11. Differences between furnace and sample maximum and minimum temperatures versus furnace temperature on 50 K/min tests.

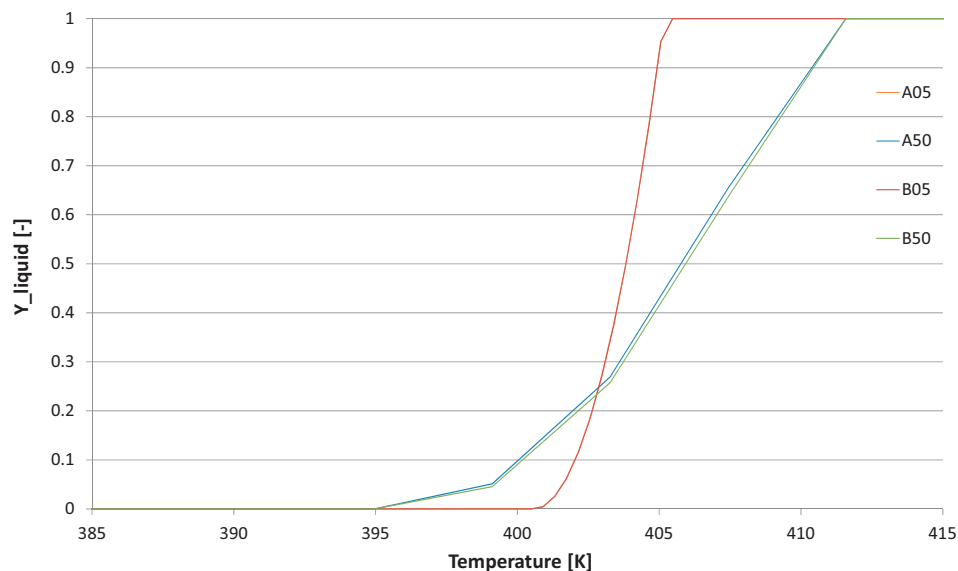**Fig. 12.** Sample temperature gradient in 50 K/min tests.

conversion. Higher heating rates resulted in a wider range of phase change temperatures, as shown in Fig. 13. The heat transfer to the sample is a possible explanation for this behaviour. Heat flux primarily depends on the crucible surface area and the temperature differences, which are very similar for both rates. Therefore, a similar heat flux is present under both rates and comparable periods of time are needed. However, during that period of time, the higher heating rate evolves over a wider furnace temperature range and the sample and furnace temperatures show a greater difference than in the lower heating rate. So, in order to estimate the phase change, a lower heating rate is advised to reduce the thermal lag. Differences in thermal diffusivity or Biot number were less important for phase change than the heating rate under simulation conditions.

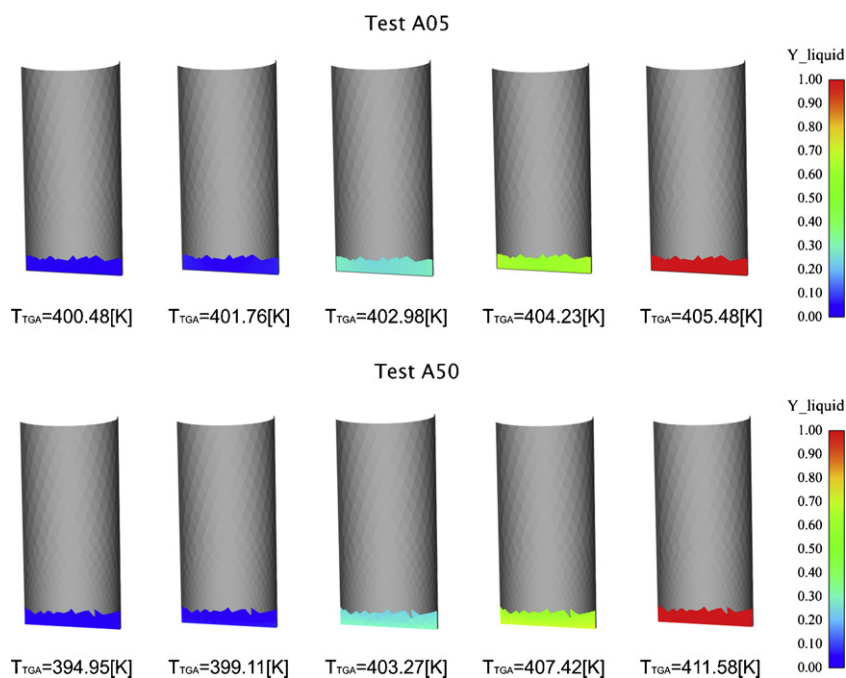This evolution of liquid fraction was also shown in Fig. 14 for 5 and 50 K/min tests.

Fig. 13. Sample liquid fraction versus furnace temperature.

Fig. 14. Sample liquid fraction contours at different furnace temperatures during A05 and A50 tests.

4. Conclusions

A simulation of a TGA-DSC device has been performed to analyse the effects of several factors on thermal lag. A virtual system has been created and configured, and models have been applied.

The results show that sample temperature was usually lower than furnace temperature for low heating rates, while the opposite situation took place for high heating rates. The temperature difference between furnace and sample underwent a peak during latent heat transfer in all the tests.

Moreover, a sample with a lower thermal diffusivity (A) had greater temperature differences when compared to the furnace temperature than a sample with a higher thermal diffusivity (B). In addition, typical conditions in the TGA-DSC lead to a higher Biot number in the sample A, implying that greater temperature differences were observed within that sample. However, the overall magnitude of this difference was small and the calculated Biot numbers allowed the sample to be considered isothermal. Under the test conditions, thermal diffusivity and Biot number effects were miniscule compared to the effect of the heating rate on phase change measurements, which increased instability between the sample and furnace temperatures and temperature differences within the sample.

Another conclusion of this work is that higher heating rates resulted in a wider range of phase change temperatures. While the heat flux needed to heat the sample is similar in both tests, the furnace temperature increasing rate is different, so a higher thermal lag arises from higher heating rates.

As a result, the thermal lag during an experimental test can be analysed based on simulation information, sample characteristics and heating rate in order to account for this effect on the obtained data.

Acknowledgement

References

[1] R. Comesaña, J. Porteiro, E. Granada, J.A. Vilán, M.A. Álvarez Feijoo, P. Eguía, CFD analysis of the modification of the furnace of a TG-FTIR facility to improve the correspondence between the emission and detection of gaseous species, Appl. Energy 89 (2012) 262–272.

[2] E. Granada, P. Eguía, J.A. Vilan, J.A. Comesaña, R. Comesaña, FTIR quantitative analysis technique for gases. Application in a biomass thermochemical process, Renew. Energy 41 (2012) 416–421.

[3] SETARAM, Labsys TG, TG-DTA and TG-DSC Documentation, 2005.

[4] R. Narayan, M.J. Antal Jr., Thermal lag, fusion, and the compensation effect during biomass pyrolysis, Ind. Eng. Chem. Res. 35 (1996) 1711–1721.

[5] M.-K. Bahng, C. Mukarakate, D.J. Robichaud, M.R. Nimlos, Current technologies for analysis of biomass thermochemical processing: a review, Anal. Chim. Acta 651 (2009) 117–138.

[6] T. Fisher, M. Hajaligol, B. Waymack, D. Kellogg, Pyrolysis behavior and kinetics of biomass derived materials, J. Anal. Appl. Pyrolysis 62 (2002) 331–349.

[7] A.M.C. Janse, R.W.J. Westerhout, W. Prins, Modelling of flash pyrolysis of a single wood particle, Chem. Eng. Process. 39 (2000) 239–252.

[8] E.L.K. Mui, W.H. Cheung, V.K.C. Lee, G. McKay, Compensation effect during the pyrolysis of tyres and bamboo, Waste Manage. 30 (2010) 821–830.

[9] L. Liu, Q.X. Guo, Isokinetic relationship, isoequilibrium relationship, and enthalpy–entropy compensation, Chem. Rev. 101 (2001) 673–695.

[10] P. Budrugeac, On the pseudo compensation effect due to the complexity of the mechanism of thermal degradation of polymeric materials, Polym. Degrad. Stab. 58 (1997) 69–76.

[11] K. Nobuyoshi, A review of the mutual dependence of Arrhenius parameters evaluated by the thermoanalytical study of solid-state reactions: the kinetic compensation effect, Thermochim. Acta 244 (1994) 1–20.

[12] M. Grønli, M.J. Antal Jr., G. Várhegyi, A round-robin study of cellulose pyrolysis kinetics by thermogravimetry, Ind. Eng. Chem. Res. 38 (1999) 2238–2244.

[13] M.J. Moran, H.N. Shapiro, Fundamentals of Engineering Thermodynamics, John Wiley & Sons, Inc., Hoboken, NJ, USA, 2000.

[14] K.J. Åström, T. Hägglund, PID Controllers, International Society for Measurement and Control, Research Triangle Park. USA, 1995.

[15] K. Ogata, Modern Control Engineering, 4th edition, Prentice Hall, Upper Saddle River, NJ, USA, 2001.

[16] Mathworks, Matlab 7.10.0 Documentation, 2010.

[17] Fluent Inc., Fluent 12.1.4 Documentation. User's Guide, 2009.

[18] R. Artiaga, S. Naya, A. García, F. Barbadillo, L. García, Subtracting the water effect from DSC curves by using simultaneous TGA data, Thermochim. Acta 428 (2005) 137–139.